Energy Reports 11 (2024) 2991–3004

Contents lists available at ScienceDirect

Energy Reports

journal homepage: www.elsevier.com/locate/egyr

Research paper

Hydrodynamic characteristics of wing-in-ground effect oscillating hydrofoil on power extraction performance

Weijie Mo [a], Guanghua He [a,b,c,*], Jian Wang [c], Zhigang Zhang [c], Jiadong Wang [d], Pengfei Liu [e], Hassan Ghassemi [c,f], Hao Yang [a]

[a] School of Mechatronics Engineering, Harbin Institute of Technology, Harbin 150001, China
[b] Shandong Institute of Shipbuilding Technology, Weihai 264209, China
[c] School of Ocean Engineering, Harbin Institute of Technology, Weihai, Weihai 264209, China
[d] Department of Mechanics, Zhejiang University, Hangzhou 310027, China
[e] Marine, Offshore and Subsea Technology, School of Engineering, University of Newcastle Upon Tyne, UK
[f] Department of Maritime Engineering, Amirkabir University of Technology, Tehran, Iran

ARTICLE INFO

Keywords:
Current energy
Oscillating hydrofoil
Hydrodynamic
Wing-in-ground effect

ABSTRACT

The energy contained in the tidal motion of the seas and oceans has the potential to be a significant source of renewable energy. The oscillating hydrofoil current-energy turbine has a good performance to extract energy from the coupling of its heaving and pitching motions. In the present study, the wing-in-ground (WIG) effect has been considered to improve the power-extraction performance of the oscillating hydrofoils. The overset grid in the commercial computational fluid dynamic (CFD) software STAR CCM+ is applied to study the flapping hydrofoil with dynamic WIG effect between two hydrofoils. The simulation results show that the WIG effect can greatly improve the power extraction performance of the flapping hydrofoil. The WIG effect is asymmetric over the course of the foil moving toward or leaving from the symmetry plane. The distance of the gap has a major influence on the hydrodynamic performances of the flapping hydrofoil. For a moderate gap, the positive pressure on the lower surface enhances as the hydrofoil departs from the symmetry plane and causes an improvement of lift and moment coefficients. As the gap decreases further, the increasing negative pressure between the leading edge and the symmetry plane plays an essential role improving the power extraction as the hydrofoil approaches the symmetry plane. Compared to the case without the WIG effect, the power-extraction efficiency has an increment of 16.34% in the present study.

1. Introduction

The development of clean renewable energy resources is urgent as increasing consumption of fossil energy and resulting environmental pollution and the over-exploitation. A mix of renewable strategy is required to satisfy the increasing demand for power. Wind is estimated to have a huge potential, which is reflected in the rapid growth of wind power industry. However, water (including rives and tidal currents) has an advantage of being predictable, especially for a tidal current energy which has abundant resources.

According to the type of the generator, the tidal current power generation devices can be roughly divided into two groups: rotary blades and flapping hydrofoils designs. The rotary blades design is traditional with a proven technology for decades; comparatively, the flapping hydrofoils design is gradually becoming a new hotspot. The flapping-hydrofoil power generator has some key potential advantages, such as a low kick-in speed, less influenced by the non-uniformity of flow and low foil velocities (and hence less impact on the surrounding environment and lower noise). Compared with the rotary-blade turbines, the flapping hydrofoils can achieve a higher efficiency at a low flow speed (Young et al., 2014).

The idea of utilizing the flapping foils comes from the bionics, such as the bird flying and fish swimming. A bird can obtain the thrust and lift simultaneously through a regular swing wings motion. Mckinney and Delaurier (1981) first conducted an experimental study on the swing-wing windmill in 1981, and found that 90 degrees is the most efficient phase difference between the pitch and heave motions. Jones and Platzer (1997) predicted the energy extraction efficiency of an

* Corresponding author at: School of Mechatronics Engineering, Harbin Institute of Technology, Harbin 150001, China.
E-mail address: ghhe@hitwh.edu.cn (G. He).

https://doi.org/10.1016/j.egyr.2024.02.052
Received 12 November 2022; Received in revised form 30 May 2023; Accepted 26 February 2024
Available online 29 February 2024
2352-4847/© 2024 The Authors. Published by Elsevier Ltd. This is an open access article under the CC BY-NC license (http://creativecommons.org/licenses/by-nc/4.0/).

airfoil considering the heave and pitch motions simultaneously in an unsteady, inviscid and incompressible two-dimensional flow. Simpson (2009) used a dimensionless reduced frequency to describe the regions of power-extraction efficiency and marked the distribution of vortices in different regions at $Re = 13{,}800$.

To improve the power-extraction efficiency, Young et al. (2013) proposed a non-sinusoidal motion, which can generate a higher efficiency than that of a sinusoidal motion at a large pitching angle. The non-sinusoidal motion causes the leading-edge vortex acting on the hydrofoil to be at a more appropriate location and timing, further resulting in the increase of the power extraction. The reattachment of separating leading-edge vortex improves the power extraction efficiency. However, the control of this effect is difficult to provide a stable result in three-dimensional flow (Deng et al., 2014).

Kinsey and Dumas (2008) studied the parameter sensitivity on the two-dimensional oscillating-airfoil energy efficiency at a low Reynolds number, and the results indicate that the system has the highest energy efficiency when the amplitude of the pitching motion is about 75 degrees and the reduced frequency f^* is about 0.15. The experimental results (Kinsey et al., 2011) also indicate that the energy efficiency for the single hydrofoil and dual-hydrofoil neglecting the mechanical losses is about 30%, 40%, respectively. They conducted three-dimensional numerical studies on the two oscillating hydrofoils arranged in series and found that the vortices induced by the upstream flapping hydrofoil have beneficial effects on the energy efficiency of the downstream hydrofoil (Kinsey and Dumas, 2012). Kinsey and Dumas (2014) studied the energy efficiency of a flapping hydrofoil and found that the maximum efficiency is 43% when $Re = 5\times10^5$. Recently, they had a further study of a foil oscillating with large heaving amplitudes (Picard-Deland et al., 2019). A new pitching trajectory subjected to more flatting profiles of effective angle of attack was proposed to improve the energy-extraction performance of foil, and the efficiency can be reached up to 49%.

The vortex interactions for a tandem configuration were also studied using a potential flow method. Xu and Xu (2017) found that the power-extraction performance of the downstream foil is highly dependent on the globe phase shift, which is combined with the longitudinal distance and the phase shift of the motions of the two foils. This conclusion has a good agreement with Kinsey's results (Kinsey, 2012) using a CFD commercial code ANSYS Fluent.

Besides the fully active flapping foil, there is a much simpler and challenging concept of a fully passive flapping foil turbine. Duarte et al. (2019) conducted a rigorous experiment exploring the optimal structural parameters for energy harvesting, and four conceptually different responses have been experimentally observed. Their work provides an important reference for the structural design. Then Duarte et al. (2021) proposed a strong fluid-solid coupling strategy to simulate a lightweight flapping foil, avoiding the well-known added-mass instability. Theodorakis et al. (2022) investigated the performance of a fully passive flapping foil under sheared inflow condition, however, the power-extraction improvement is relatively small. They further considered the influence of free-surface and found that the energy harvesting performance of flapping foil deteriorated significantly.

Engineering Business Ltd. built the first commercial flapping-hydrofoil turbine with 150 kW "Stingray" prototype in 2003 in Scotland (The Engineering Business Limited, 2002, 2003, 2005). It generated a maximum production of 85 kW with a moderate power efficiency of 11.5%, showing that the power efficiency was unsatisfactory. Pulse Tidal Ltd. tested a dual-hydrofoils 100 kW prototype turbine in the UK (Pulse Tidal Ltd., 2011). How to improve the power-extraction efficiency of the flapping-hydrofoils is an urgent topic deserving further study.

From this regard, we studied the WIG effect, which may be a good method to increase energy efficiency. The WIG effect, also known as the wing-ground effect or wing-surface effect, usually refers to the ground effect on the flow characteristics of air around the aircraft when it approaches the ground (Luo and Chen, 2012). An aircraft flying at a low altitude can induce the WIG effect, and a racing car at a high speed applies a WIG effect to increase the downforce. Molina and Zhang (2011) investigated the WIG effect of the inverted airfoil with the heave motion and obtained three regimes with different motion frequencies. Caused by the WIG effect, the downforce will be increased owing to a Venturi channel being created between the lower surface and the ground. However, for a low ride height, the Venturi effect cannot overcome the effect of separation and the airfoil stalls.

Recently, the WIG effect has been introduced in flapping hydrofoil devices. Jones and Platzer (2002) studied the WIG effect on the flapping hydrofoil propulsion device in both experimental and numerical methods. Liu et al. (2010) studied the propulsion efficiency of the WIG propulsion device and found that, compared with the traditional screw propeller, the device can be used at a higher speed. Wang et al. (2020) conducted a parametric study on the propulsive performance of the auto-pitch wing-in-ground effect oscillating foil propulsors (APWIGs). The maximum propulsive efficiency of 12% is induced by the WIG effect. APWIGs can reach up to a high efficiency of 70% when the corresponding parameters are selected appropriately.

Zhu et al. (2009) studied the WIG effect with an average distance of 0.25 and 0.5 chord length between the hydrofoil and the ground in both two-dimensional and three-dimensional inviscid numerical methods. They found that the presence of the ground could improve the heaving response, power extraction and efficiency significantly. The maximum energy-extraction efficiency without the ground was 8%, by contrast, it can be increased to about 17% when considering the WIG effect.

Liu (2015) used a boundary element method to study the energy-extraction efficiency of the hydrofoil considering the WIG effect. The results show that the dynamic WIG effect produced 18% more energy annual when the gap between two wings is 0.2 chord length. Compared with a single foil, the WIGT (Wing-in-ground effect turbine) with proper motion and geometry parameters can generate 5 times power. However, Moryossef and Levy (2004) conducted a comparison of the inviscid and viscous turbulent flow simulations for oscillating airfoils near the ground. The comparison shows that the results based on the inviscid assumption are only valid for a moderate-high distance (about $0.5c$) from the ground. This phenomenon means that when the distance is smaller than $0.5c$, it looks like the extreme ground effect, rather than the ground effect, further implying that the viscous effect cannot be neglected. The inviscid efficiency results may be much larger than the viscid results.

Zhu et al. (2020) used a dynamic mesh with a sliding interface to study the ground effect when the average distance from the foil to the ground has the smallest value of $1.4c$. They mentioned that the ground effect has asymmetric characteristics when the flapping foil goes toward and away from the ground wall. The pressure in the suction side has an obvious decrease and leads to an overall increase in the heaving force. They found that the maximum efficiency is obtained when the gap $h = 2.8c$ with an increase of 13.87% compared to the case ignoring the ground effect. The ground effect decreases as the flow is transferred from laminar to turbulent with the increased Reynolds number.

Abiru and Yoshitake (2012) experimentally investigated the hydro-elastic response of the semi-active wing with an exciting pitching oscillation. Further, for discussing the influence of neighboring wings in a parallel arrangement, they used a practical cascade wing generator using two experimental devices. Induced by the antiphase oscillating of neighboring foils, the efficiency will improve by approximately 15% and 20–30% when the gap is twice and 1.5 times the chord length, respectively. This improvement of the parallel arrangement should be attributed to the dynamic WIG effect between two flapping hydrofoils.

In the present work, the hydrodynamic characters and power extraction performance of the flapping hydrofoil under the WIG effect are investigated, especially for an extreme small gap between the two hydrofoils. Initially, the uncertainty analysis estimations are made with respect to the cell grid and time step. The comparisons with the available numerical results are performed, including a single foil case and a WIG

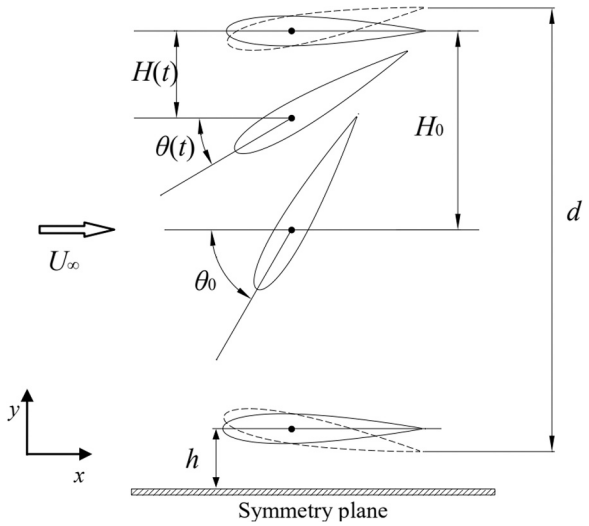

Fig. 1. Diagram of motions of the oscillating hydrofoil.

effect case. Afterwards, the WIG effect is investigated with different parameters and the optimal power-extraction efficiency is found. The Venturi effect is discovered at an extreme small gap, which contributes greatly to the power-extraction. Finally, we compare the results for different pitching axis positions under WIG effect.

2. Numerical model

The flapping hydrofoil can be regarded as a two-degree-of-freedom (DOF) system, including the heaving and pitching motions. The rotation center of the pitching motion is located at x_p, which denotes the distance from the leading edge to the pitching axis. The chord length of the hydrofoil is defined as c. In the present study, the value of 0.25 m was selected for c. The phase difference φ between the heaving and pitching motions is selected as 90°, which is relatively optimal in the previous studies (Young et al., 2014; Kinsey and Dumas, 2008). The equations of the heaving and pitching motions of the hydrofoil are expressed as follows:

$$H(t) = H_0 \sin(2\pi ft + \varphi) \tag{1}$$

$$\theta(t) = \theta_0 \sin(2\pi ft) \tag{2}$$

where H_0 and θ_0 are the heaving and pitching amplitudes, respectively; f is the motion frequency, and $f^* = cf/U_\infty$ is the dimensionless reduced frequency.

The motions of the hydrofoil are given in Fig. 1. Since the two hydrofoils move symmetrically, we use the symmetry boundary condition conducting the simulations. The bottom line in Fig. 1 represents the symmetry plane between two hydrofoils, and the distance h is defined as the distance from the plane to the pitching axis when the hydrofoil reaches the horizontal position at $t/T = 0.5$. U_∞ is the uniform inflow velocity, and d is the maximum sweep height of the hydrofoil. The hydrodynamic coefficients including the dimensionless vertical force coefficient C_Y (t), horizontal coefficient C_X (t) and pitching moment coefficient C_m (t) can be formulated as:

$$\begin{aligned} C_Y(t) &= 2Y(t)/\rho U_\infty^2 c \\ C_X(t) &= 2X(t)/\rho U_\infty^2 c \\ C_m(t) &= 2M(t)/\rho U_\infty^2 c^2 \end{aligned} \tag{3}$$

Here, Y (t), X (t), M (t) are the instantaneous values of the vertical force, horizontal force and moment of the hydrofoil, respectively. The direction of the vertical force Y (t) is perpendicular to the inflow, whereas the horizontal force has the same direction as the inflow. Further, the positive direction of the moment is nose-down, namely counterclockwise.

The power coefficient C_P of the energy extraction by the oscillating hydrofoil is expressed as:

$$C_P(t) = 2P(t)\Big/\rho U_\infty^3 c = \frac{1}{U_\infty}\left[C_Y(t)\frac{dh(t)}{dt} + C_m(t)c\frac{d\theta(t)}{dt}\right] \tag{4}$$

where P (t) is the instantaneous power of the hydrofoil. The average power coefficient $\overline{C_P}$ over one cycle is defined as:

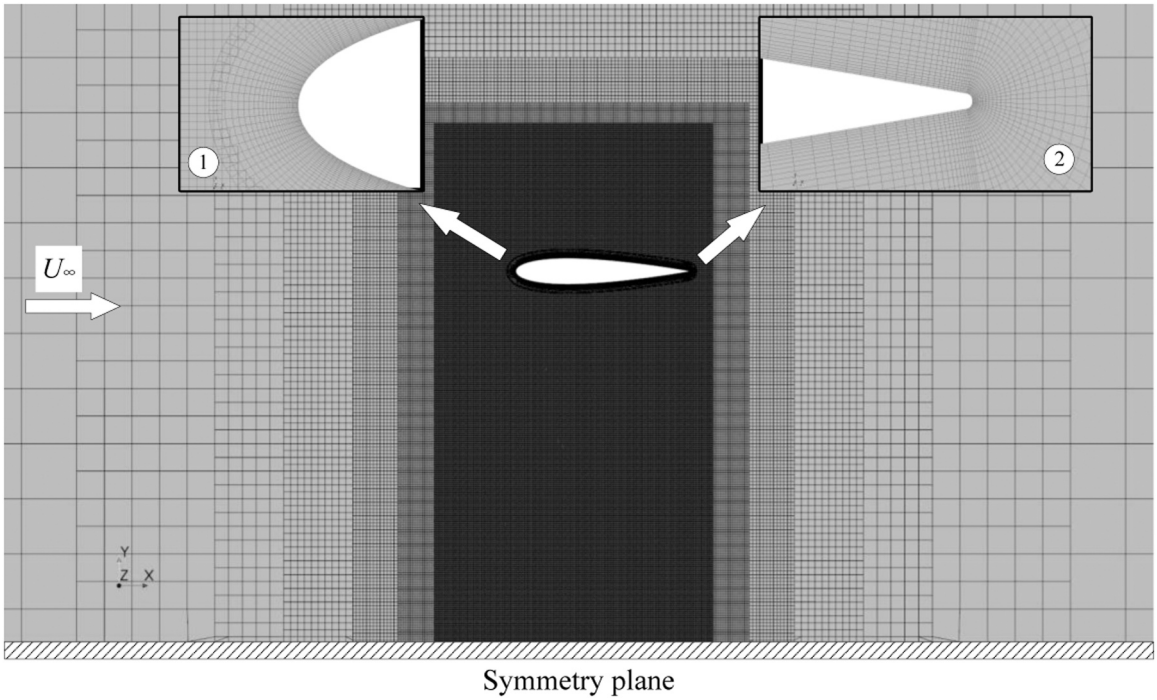

Fig. 2. Mesh generation. — ①, ② are the detailed figures of the leading edge and trailing edge.

Table 1
The setup of cell number of grid and time step for the convergence study.

Convergence Setup	Grid Cell	Time Step
Fine(S_1)	3.2E5	T/3200
Medium(S_2)	1.6E5	T/1600
Coarse(S_3)	8.0E4	T/800

$$\overline{C_P} = \frac{1}{T}\int_0^T C_P(t)dt = 2\overline{P}\Big/\rho U_\infty^3 c \tag{5}$$

where T is the one period, and the efficiency of system capacity is given as follow:

$$\eta = 2\overline{P}\Big/\rho U_\infty^3 d = \overline{C_P}\frac{c}{d} \tag{6}$$

where d is the overall extend of the foil motion shown in Fig. 1. We define the power available as the flux of kinetic energy flowing through the overall area swept by any part of the foil during its motion cycle. To operate in the power extraction regime requires a large pitching amplitudes, the distance d is usually larger than $2H_0$. This definition is also recommended and used by the groups (Deng et al., 2014; Zhu et al., 2009). The maximum energy extraction efficiency is limited to 59% according to the Betz' law, which is independent of the design of a wind turbine in open flow.

3. Numerics

The commercial software STAR CCM+ is used to solve the unsteady Reynolds-averaged Navier-Stokes (URANS) equations. An incompressible separation flow solver combined with the semi-implicit method for pressure linked equations (SIMPLE) algorithm and the one-equation Spalart-Allmaras turbulence model have been employed in the present study (Nishino et al., 2008; Zerihan, 2001).

The computational domain is a rectangular region with a size of 70c (x-direction) × 70c (y-direction). The overset mesh function is used in the STAR-CCM+ to make the moving foil's mesh superimpose with the static background mesh. The background mesh is an unstructured mesh, which is generated in STAR CCM+. It is gradually refined near the surface of the moving foil. By contrast, the mesh for the moving foil is generated using O-grid meshes, and $y+$ is set to 1. The boundary condition, which connects the background mesh with the moving foil's mesh, is set as the overset mesh. The meshes for the partially significant foil edge are enlarged, as given in Fig. 2. There are totally 437 nodes on the foil surface, which is fine enough for the study (Kinsey and Dumas, 2008, 2012). The number of the cells in the body-fitted mesh is 12702. The thickness of the body-fitted mesh is about 0.06c. Moreover, the size of the outside boundary (overset boundary) of the body-fitted mesh is about $\Delta x = 0.0015(0.006c)$. The interpolation scheme for the space is linear interpolation with a second-order precision.

The inflow velocity U_∞ and Reynolds number are 2 m/s and 500,000, respectively. A symmetrical foil of NACA 0015 is selected for the calculation. The heaving amplitude H_0 of the oscillating hydrofoil is selected as one chord length and the optimal cases are obtained for a heaving amplitude on the order of the chord length (Kinsey et al., 2007). The pitching amplitude θ_0 is selected as 60 degrees to avoid collision between the two foils (Liu, 2015). The motion frequency is 1.12 Hz and the reduced frequency f^* is 0.14 which is a relatively optimal value in the study (Simpson, 2009; Deng et al., 2014; Zhu, 2011).

3.1. Uncertainty analysis estimation

An uncertainty analysis estimation with respect to both the time step and grid size was carried out using the correlation factor method (Stern et al., 2001; Wilson et al., 2001) with $f^* = 0.14$, $\theta_0 = 75°$, $H_0 = c$. In order to evaluate the numerical uncertainties, three solutions with systematically refined time step or grid size were conducted. When the convergence study of one input parameter was performed, all other input parameters were kept constant. The numerical setup for the convergence study is shown in Table 1, in which the uniform refinement ratio of 2 and$\sqrt{2}$for the time step and grid size are used, respectively.

The current study follows the procedure by Stern et al. (2010) to estimate the numerical uncertainties with respect to the time step and grid size. Time-averaged horizontal force and power coefficients are selected as the integral variables to perform the uncertain calculation. It is assumed that iterative errors are negligible compared with the time-step and grid-size convergence errors in this study. Therefore, the numerical errors are decomposed into the contributions from the time step and grid size. The changes of horizontal force and power coefficients between fine, medium and coarse solutions for kth input parameter can be calculated as:

$$\varepsilon_{k21} = S_2 - S_1 \tag{7}$$

$$\varepsilon_{k32} = S_3 - S_2 \tag{8}$$

where S_1, S_2 and S_3 correspond to solutions with fine, medium and coarse input parameter, respectively. The convergence ratio is defined as the changes between the medium-fine and coarse-medium solutions:

Table 4
Independence study of the computational domain with three different sizes. —$f^* = 0.14$, $\theta_0 = 60°$, $H_0 = c$, $Re = 500{,}000$.

Domain size ($c\times c$)	$\overline{C_X}$	$\widehat{C_Y}$	$\widehat{C_m}$	$\overline{C_P}$	η%
50×50	0.873	2.093	0.385	0.610	25.42 (0.5%)
70×70	0.871	2.093	0.386	0.608	25.33 (0.2%)
75×75	0.869	2.086	0.384	0.607	25.29 (~)

Table 2
Numerical uncertainty for grid size.

Variable	Solution			Convergence Ratio	Uncertainty		
	S_{G1}	S_{G2}	S_{G3}	R_G	δ^*_G (S_{G1}%)	U_G (S_{G1}%)	U_{Gc} (S_{G1}%)
$\overline{C_X}$	1.808	1.796	1.768	0.167	0.664	1.195	0.530
$\overline{C_P}$	0.975	0.974	0.969	0.200	0.102	0.179	0.077

Table 3
Numerical uncertainty for time step.

Variable	Solution			Convergence Ratio	Uncertainty		
	S_{T1}	S_{T2}	S_{T3}	R_T	δ^*_T (S_{T1}%)	U_T (S_{T1}%)	U_{Tc} (S_{T1}%)
$\overline{C_X}$	1.796	1.782	1.727	0.250	0.260	0.294	0.027
$\overline{C_P}$	0.974	0.986	1.013	0.444	0.411	2.136	0.575

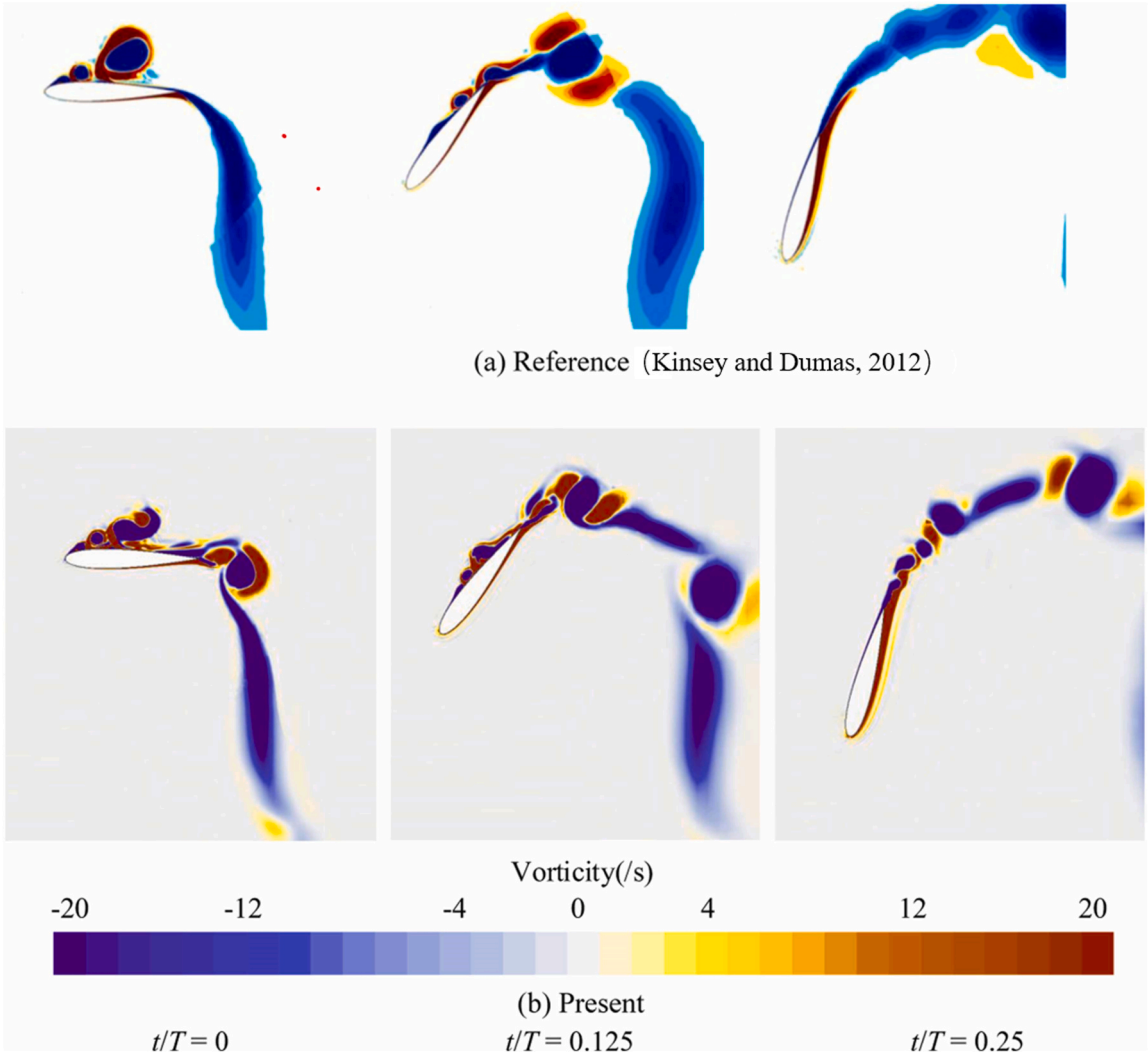

Fig. 3. Comparisons of the vorticity fields at three-time instants ($t/T = 0$, 0.125, 0.25). —$f^* = 0.14$, $\theta_0 = 75°$, $H_0 = c$, $Re = 500{,}000$.

$$R_k = \frac{\varepsilon_{k21}}{\varepsilon_{k32}} \tag{9}$$

Convergence ratio is employed to determine the convergence conditions, which include (i) monotonic convergence ($0 < R_k < 1$), (ii) oscillatory convergence ($R_k < 0$; $|R_k| < 1$), (iii) monotonic divergence ($R_k > 1$), (iv) oscillatory divergence ($R_k < 0$; $|R_k| > 1$).

For the condition (ii), numerical uncertainties are predicted by bounding the error based on oscillation with maximum and minimum solutions. The errors and uncertainties cannot be estimated for condition (iii) and (iv). With respect to the condition (i), numerical errors and uncertainties are estimated by generalised Richardson extrapolation, which provides the estimate for one-term numerical error and order of accuracy as following equations:

$$\delta^*_{REk1} = \frac{\varepsilon_{k21}}{r_k^{p_k} - 1} \tag{10}$$

$$p_k = \frac{\ln(\varepsilon_{k32}/\varepsilon_{k21})}{\ln(r_k)} \tag{11}$$

where r_k is the uniform refinement ratio for kth input parameter. Correction of Eq. (10) through a multiplication factor C_k accounts for effects of higher-order terms:

$$\delta^*_k = C_k \delta^*_{RE_{k1}} \tag{12}$$

where the correction factor is given by

$$C_k = \frac{r_k^{p_k} - 1}{r_k^{p_{kest}} - 1} \tag{13}$$

where p_{kest} is an estimate for the limiting order of accuracy. An improved error estimate can be obtained based on the multiplication of Eq. (12) by the correction factor:

The uncorrected uncertainty U_k and corrected uncertainty U_{kc} are estimated by following equations depending on the distance of solutions to the asymptotic range:

$$U_k = \begin{cases} \left(9.6(1-C_k)^2 + 1.1\right)\left|\delta^*_{REk1}\right| & |1 - C_k| < 0.125 \\ \left(2|1-C_k| + 1\right)\left|\delta^*_{REk1}\right| & |1 - C_k| \geq 0.125 \end{cases} \tag{14}$$

$$U_{kc} = \begin{cases} \left(2.4(1-C_k)^2 + 0.1\right)\left|\delta^*_{REk1}\right| & |1 - C_k| < 0.25 \\ \left(|1-C_k|\right)\left|\delta^*_{REk1}\right| & |1 - C_k| \geq 0.25 \end{cases} \tag{15}$$

Results of numerical uncertainty for mesh and time step are listed in Tables 2 and 3. The convergence ratios obey (i) monotonic convergence condition. Reasonable low level of uncertainty referring to both the time step and grid size was obtained for two integral coefficients. The average horizontal force coefficient is more sensitive to the grid size resolution, while the average power coefficient tends to be more sensitive to the time step resolution. The maximum uncertainty is about 2.136% for

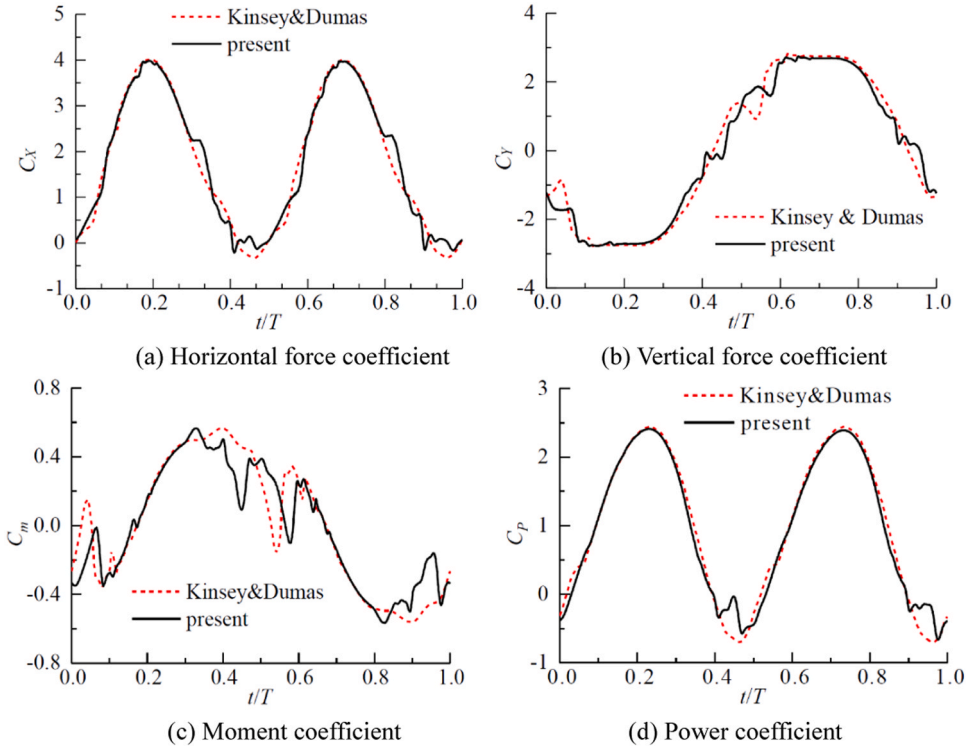

Fig. 4. Comparison of instantaneous force, moment and power extraction curves between the two simulations. —$f^* = 0.14$, $\theta_0 = 75°$, $H_0 = c$, $Re = 500{,}000$.

Table 5
Comparisons of peak force, average force and power extraction coefficients between two results. —$f^* = 0.14$, $\theta_0 = 75°$, $H_0 = c$, $Re = 500{,}000$.

	$\widehat{C_Y}$	$\widehat{C_m}$	$\overline{C_X}$	$\overline{C_P}$	η%
Reference (Kinsey et al., 2011)	2.819	0.565	1.757	0.986	38.68(~)
present	2.774	0.566	1.808	0.975	38.25 (−1.1%)

average power coefficient in the time step convergence calculation. It is worth noticing that the numerical error and uncertainties are very small, which can be neglected. The good agreement between fine and medium discretization results led us to adapt the medium grid cell resolution and time step in the following studies.

3.2. Independence relative to the domain size

The grid strategy above is followed to explore the domain size independence. Three different domain sizes were selected for calculation. The results in the second oscillation cycle after the stabilized computations are listed in Table 4. The results using the three domains are quite close in the peak values of the lift force (C_Y) and power extraction efficiency (η). A relative difference of 0.05% for C_Y is obtained between the cases of 75c×75c and 70c×70c. The power extraction efficiency η for the medium and large size domains almost have the same values. The blockage ratio of the medium size is about 2.86%, which is less than 5%. Therefore, to provide a good compromise between the precision and required time, the medium size 70c×70c is chosen for the following study.

3.3. Validation

The current numerical results are compared with the Kinsey and Dumas (2012). The grid resolution in the wake region has been refined. A good agreement of the vorticity fields at three different times has been found, as shown in Fig. 3. The vorticity fields show that the leading-edge vortex is moved to the trailing edge along the upper surface when $t/T =$

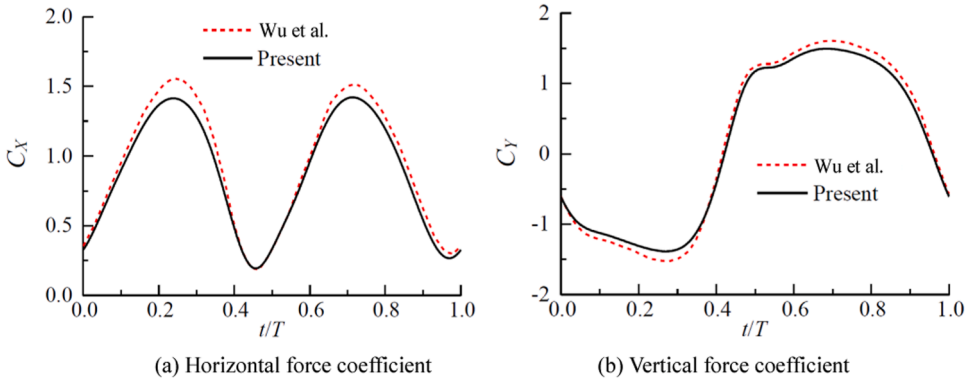

Fig. 5. Comparison of lift and drag coefficient curves under wing-in-ground effect. —$Re = 150$, $H_0 = 0.4c$, $\theta_0 = 45°$, $h = 1c$.

Table 6
Average horizontal force and power extraction coefficients with different minimum gaps h/c at $x_p = c/3$. —$f^* = 0.14$, $\theta_0 = 60°$, $H_0 = c$, $Re = 500{,}000$.

h/c	$\overline{C_X}$	$\overline{C_P}$	η (%)
0.25	0.890	0.648	27.05(6.79%)
0.40	0.891	0.649	27.05(6.79%)
0.50	0.889	0.647	26.97(6.47%)
0.70	0.887	0.642	26.77(5.68%)
1.00	0.883	0.635	26.47(4.50%)
30.00	0.871	0.608	25.33(~)

Table 7
Numerical uncertainty for time step with three different gaps h/c at $x_p = c/3$.

h/c	δ^*_T	U_T	U_{Tc}
0.25	0.010%	0.017%	0.007%
0.40	0.026%	0.036%	0.010%
0.50	0.016%	0.029%	0.004%

0, and the vortex is gradually separated from the foil from t/T = 0.125–0.25. The predicted timing and position of the flow separation are almost the same for the two results. Moreover, more detailed vorticity fields near the hydrofoil probably caused by a finer mesh around the hydrofoil are studied. The profiles of overset boundary appear, although it has a little effect on the results.

Fig. 4 shows the instantaneous values of the force, moment and power extraction coefficients in one cycle. The profiles of the two results have very similar trends in one cycle with little differences in partial inflexion points. There exists several small fluctuations in our predicted results, which are caused by the small vortex shedding from the foil surface.

The comparison of the power extraction is given in Table 5. The computational results are very close. The differences in the peak vertical force coefficient and power extraction coefficient are less than 1.6% and 1.1%, respectively. Furthermore, the maximum error of the horizontal force coefficient is within 3%.

To have a further validation of the results considering the WIG effect, a comparison with Wu's results by the Immersed Boundary-Lattice Boltzmann Method (IB-LBM) is provided in Fig. 5 (Wu et al., 2014). The vertical and horizontal force coefficients over one cycle for the two different results almost have the same values. The differences between them are very small with variations of less than 7% on peak vertical force coefficients.

4. Results

After the uncertainty analysis estimation and validation of the employed numerical method, the comprehensive demonstration of power extraction characteristics for flapping foil with WIG effect is performed. The basic configurations are: NACA 0015 foil, $Re = 500{,}000$, $H_0/c = 1$, $f^* = 0.14$, and $\theta_0 = 60°$. The pitching axis is located at $x_p = c/3$. It should be noticed that for present condition of $f^* = 0.14$, $\theta_0 = 60°$, there is no significant leading edge vortex as shown in Fig. 3 due to the relatively small angle of attack. When the gap h between the foil and the symmetry plane is varied from 0.25c to 30c (h is shown in Fig. 1), the numerical results of the averaged horizontal force, power extraction coefficient and efficiency are listed in Table 6. A large gap of $h = 30c$ is selected as a typical case without the WIG effect, and its power-extraction efficiency can be reached to 25.33%. As the gap h decreases, the average values $\overline{C_X}$, $\overline{C_P}$ and efficiency η all have gradual increasing trends. When the gap h equals to 0.25c, the optimal efficiency

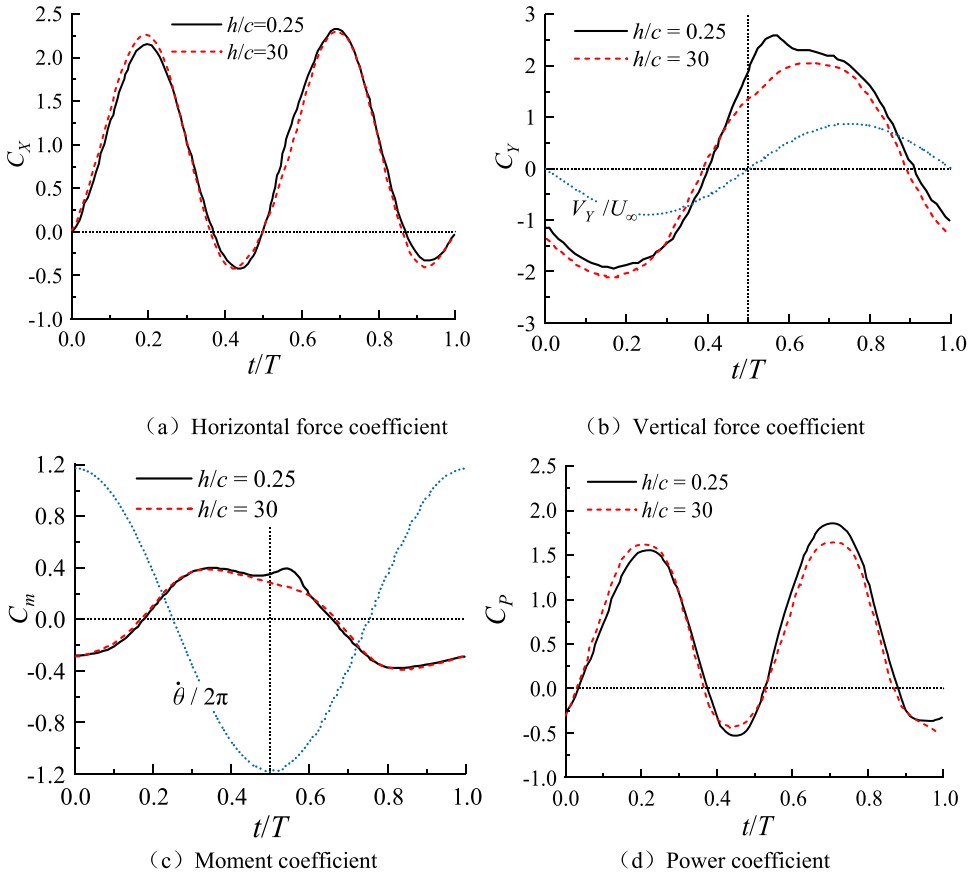

Fig. 6. Comparison of instantaneous force, moment and power coefficients for a single hydrofoil with or without WIG effect. —$f^* = 0.14$, $\theta_0 = 60°$, $H_0 = c$, $Re = 500{,}000$.

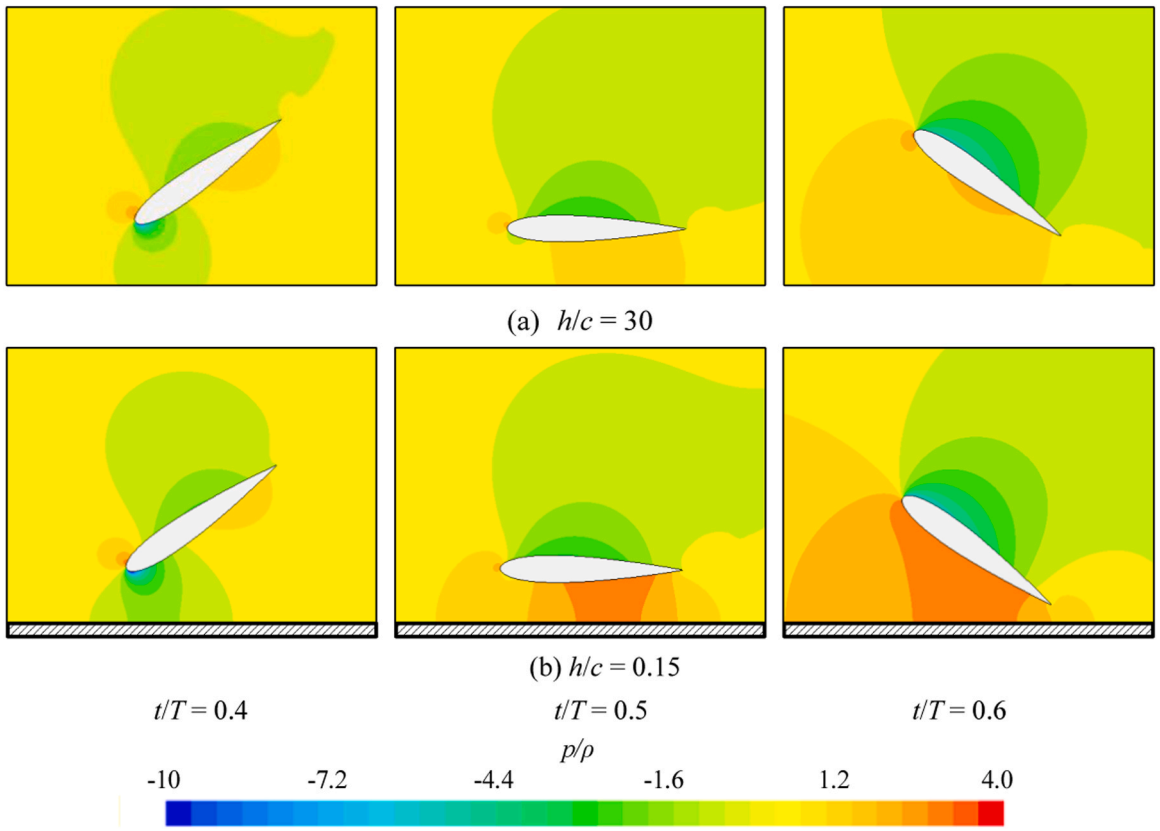

Fig. 7. Comparison of the pressure distributions with/without the WIG effect at $t/T = 0.4, 0.5, 0.6$. — $f^* = 0.14$, $\theta_0 = 60°$, $H_0 = c$, $Re = 500{,}000$, $x_p = c/3$.

Table 8
Average power extraction coefficients with different phase φ at $x_p = c/3$.

φ	$\overline{C_{PY}}$	$\overline{C_{Pm}}$	$\overline{C_P}$	η %
80°	0.707	-0.152	0.555	23.20
90°	0.807	-0.158	0.649	27.05
100°	0.799	-0.164	0.635	26.55

can reach up to 27.05% due to the WIG effect, which has an increment of 6.79%.

We also performed an uncertainty analysis for the present cases. Three typical cases with relatively small gaps (h/c = 0.25, 0.40, and 0.50) were selected for conducting the uncertainty analysis. In Tables 3 and 4, it is shown that the averaged power coefficient is more sensitive to the time step. As listed in Table 7, the corresponding numerical errorδ_T^*, uncertainty$U_T$and corrected uncertaintyU_{Tc}all have very small values. The maximum uncertainty value is happened at the gap of h/c = 0.40 withδ_T^* = 0.026%, U_T = 0.036%andU_{Tc} = 0.010%. The results are much smaller than the corresponding values shown in Table 4. It is mainly caused by a relatively smaller pitching amplitude for the present cases. For $\theta_0 = 75°$, the hydrofoil experiences a deep dynamic stall and the forces fluctuate fiercely in one period. Comparatively, there are small force fluctuations for $\theta_0 = 60°$ with a slight dynamic stall. Thus, the uncertainty can be ignored for the cases.

The instantaneous values of the force, moment and power-extraction coefficient in one cycle at h/c = 0.25 and 30 are shown in Fig. 6. Consequently, the first peak value of the horizontal force coefficient for h/c = 0.25 is slightly smaller than that for h/c = 30. However, it is larger at t/T = 0.5–0.6. The vertical force coefficients almost have the same values before t/T = 0.4 when the foil approaches the symmetry plane, and a small peak value appears when the foil departs from the symmetry plane at about t/T = 0.5–0.7. In Fig. 7, the pressure distribution for h/c = 30 and 0.25 is compared. A high positive pressure region on the lower surface of the foil is responsible for the increment of vertical force as the foil gradually departs from the symmetry plane at t/T = 0.5–0.7, which agrees very well with the curve trend shown in Fig. 6(b). The profiles of C_Y and V_Y under WIG effect shows good timing in the sign switch over one period, resulting in positive values of total extracted power in Fig. 6 (d).

A peak value in the moment coefficient curve is occurred around t/T = 0.5–0.6, whereas the sign of angular velocity$\dot{\theta}$and C_m is opposite, causing a reduction of power extraction. The power-extraction coefficient has two peak values in one cycle. The first peak at h/c = 0.25 is smaller compared to h/c = 30, however, the second peak at h/c = 0.25 improves significantly with increasing vertical force. The beneficial effect induced by the WIG effect mainly occurs in a short period during one cycle when the foil departs from the symmetry plane, which induces a blockage happening (Su et al., 2018). The fluid flow is deflected toward the leading edge rather than trailing edge, which improves the effective angle of attack (AoA) over the procedure the foil leaving the symmetry plane.

To investigate the influence of phase difference φ between heaving and pitching in WIG effect on power extraction, the comparison results with varied φ are listed in Table 8. The g/c is set to 0.4c preventing the collision at different φ values. The maximum average power coefficient and efficiency are achieved at $\varphi = 90°$ reaching about 0.649 and 27.05%, respectively.

In Fig. 8(a), there are remarkable phase differences between the horizontal force coefficients because of the phase difference φ. When the hydrofoil approaches to the symmetry plane at about t/T = 0.4, the horizontal force has an apparent decrease as the φ decreases. For vertical force coefficients in Fig. 8(b), the peak value is achieved at $\varphi = 80°$ which the WIG effect creates a significant peak. However, the synchronization between the vertical speed and force is not well, resulting a moderate performance on power extraction. The synchronization

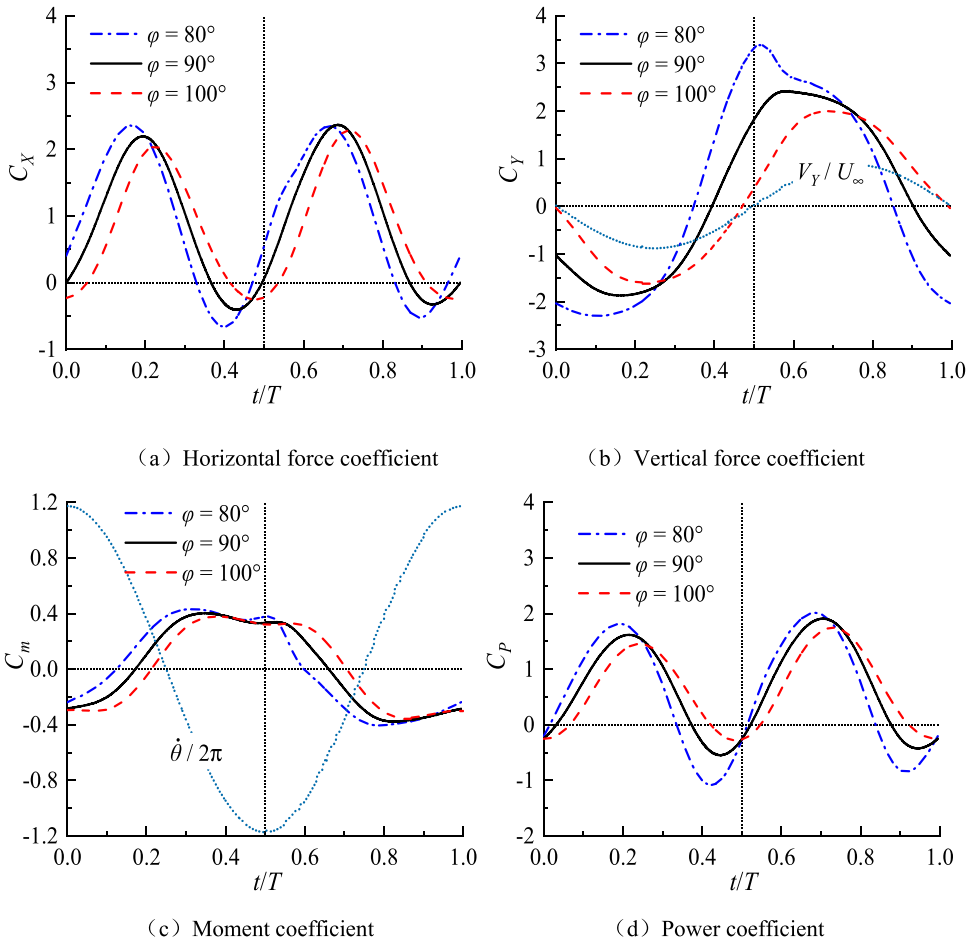

Fig. 8. Comparison of instantaneous force, moment and power coefficients for a single hydrofoil with different phase φ. —$f^* = 0.14$, $\theta_0 = 60°$, $H_0 = c$, $Re = 500{,}000$.

Table 9
Average drag force and power extraction coefficients with different minimum gaps h/c at $x_p = c/2$. —$f^* = 0.14$, $\theta_0 = 60°$, $H_0 = c$, $Re = 500{,}000$.

h/c	$\overline{C_X}$	$\overline{C_P}$	η (%)
0.15	0.840	0.670	29.90(16.34%)
0.16	0.834	0.666	29.76(15.80%)
0.18	0.828	0.661	29.48(14.71%)
0.20	0.823	0.655	29.24(13.77%)
0.24	0.811	0.643	28.70(11.67%)
0.25	0.809	0.641	28.68(11.60%)
0.30	0.802	0.634	28.32(10.19%)
0.35	0.797	0.630	28.13(9.46%)
0.40	0.794	0.627	27.97(8.83%)
0.50	0.788	0.620	27.68(7.70%)
0.70	0.780	0.611	27.24(5.99%)
1.00	0.773	0.601	26.87(4.55%)
30.00	0.759	0.578	25.70(~)

Table 10
Numerical uncertainty for time step with three different gaps h/c at $x_p = c/2$.

h/c	δ^*_T	U_T	U_{Tc}
0.15	0.071%	0.500%	0.143%
0.16	0.017%	0.013%	0.002%
0.18	0.051%	0.127%	0.025%

between the vertical speed and force is the best at $\varphi = 100°$. The good synchronization does not makes up for the deficiency in peak value. The optimal case is at $\varphi = 90°$ which qualified the advantages of synchronicity and peak value, reaching a value of $\overline{C_{PY}} = 0.807$. For the moment coefficient in Fig. 8(c), the peak value is also achieved at $\varphi = 80°$. Nonetheless, due to the poor synchronization between the C_m and $\dot{\theta}$, the consumption for pitching is minimal at $\varphi = 80°$. In Fig. 8(d), the profiles of the power coefficient indicate that the peak values increase as the φ decreases. The profile of C_P at $\varphi = 80°$ has a rapidly decrease at about $t/T = 0.4$–0.5 because of the poor synchronization of the C_Y and V_Y. The maximum value of $\overline{C_P}$ is 0.649 achieved at $\varphi = 90°$.

As the gap h decreases to smaller values, the trailing edges of two hydrofoils become more likely to crash at $x_p = c/3$. Liu (Liu, 2015) reported that the efficiency has a large increase at the $h/c = 0.16$ when using the potential flow theory. To investigate the dynamic WIG effect at a closer distance of h, the location of the pitching axis is adjusted from $c/3$ to $c/2$. The maximum sweep area d at $f^* = 0.14$, $\theta_0 = 60°$, $x_p = c/2$ is about $2.24c$, meaning that the minimum distance between the foils' trailing edge and the symmetry plane is $0.12c$. In the present study, we calculated the case at a minimum gap of $h/c = 0.15$. The horizontal force and power efficiency for different gaps with $x_p = c/2$ are shown in Table 9. As the h decreases, the horizontal force coefficient increases gradually, and the average power coefficient and power extraction efficiency have the similar increasing tendency. The efficiency can be reached up to 29.90% with an increment of 16.34% at $h/c = 0.15$.

For the three typical cases with relative small gaps ($h/c = 0.15$, 0.16, and 0.18) at $x_p = c/2$, the numerical error δ^*_T, uncertainty U_T and corrected uncertainty U_{Tc} are list in Table 10. The maximum uncertainty is

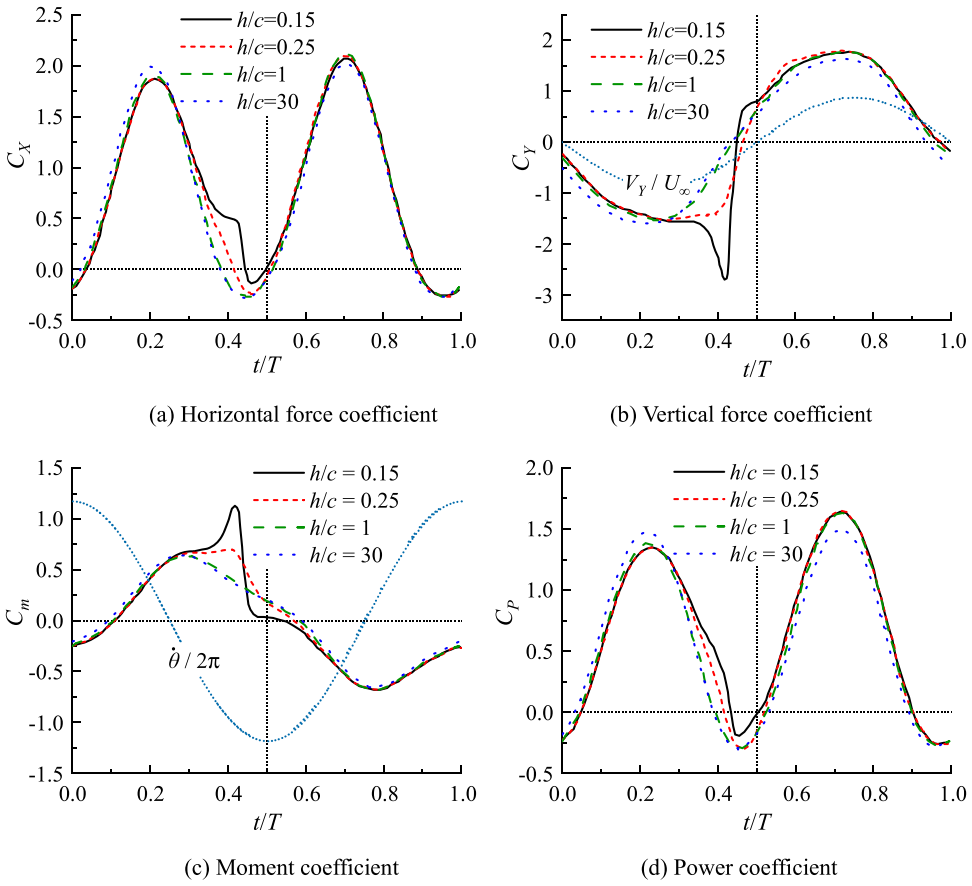

Fig. 9. Comparisons of force, moment and power coefficients with different minimum gaps h/c. —$f^* = 0.14$, $\theta_0 = 60°$, $H_0 = c$, $Re = 500{,}000$.

reached at $h/c = 0.15$ with$\delta_T^* = 0.071\%$, $U_T = 0.500\%$and$U_{Tc} = 0.143\%$, respectively. In general, the numerical errors and uncertainties for all the selected cases have very small values. The uncertainty has a moderate increase compared to the results in Table 7. As the h/c decreases, the boundary layer has an obvious separation duo to an increasing adverse pressure gradient shown in Fig. 12(b), which results in the numerical error and uncertainty both having an increasing tendency. The phenomenon contributed to larger uncertainty, however, the uncertainty can be ignored in the present study.

The comparison of force coefficients for four different gaps is given in Fig. 9. The power coefficients have significant increment when the foil approaches the symmetry plane, especially for the case at $h/c = 0.15$. It should be noted that the downforce has an apparent increase at $h/c = 0.15$ when the foil gets close to the symmetry plane at $t/T \approx 0.4$. In Fig. 10, a huge negative pressure occurs between the lower surface and the symmetry plane, which is due to the Venturi effect (Moryossef and Levy, 2004). During $t/T = 0.40$–0.45, the hydrofoil is more likely to pull towards the symmetry plane, which is induced by the negative pressure acting on the lower side instead of the positive pressure acting on the upper side. The vertical force has a significant improvement thus the power coefficient increases because the same sign of V_Y and C_Y over the period.

There is also an increment in the horizontal force caused by the increased pressure difference between the upper and lower surfaces, shown in Fig. 9(a). In addition, one notes further that the negative pressure has an unfavorable impact on the pitching contribution despite its small overall contribution. While this Venturi effect is not very evident when h/c is larger than 0.25. During $t/T = 0.5$–0.6, as the foil begins to depart from the symmetry plane, the positive pressure on the lower surface of the foil begins to be dominated due to the blockage mentioned before, the vertical force has a slighter increase and it has a relatively small impact on the power extraction.

To further investigate the pressure distribution on the surface of the hydrofoil, the pressure coefficient on both upper and lower surface at $t/T = 0.4$ is shown in Fig. 11. It is observed that there has a negative pressure at the leading edge on the lower surface for $h/c = 30$. The negative pressure on the lower surface has a steep increase at $h/c = 0.15$ with Venturi effect. The pressure on the upper surface has little difference for two conditions, comparatively. The positive pressure at the leading edge of the upper surface has a little increase at $h/c = 0.15$.

Fig. 12 shows the procedure of hydrofoil motion over one cycle with/without WIG effect, respectively. Fig. 12(a) indicates that there is not exhibiting apparent dynamic stall at $h/c = 30$ for the case without WIG effect. By contrast, the separation of the boundary layer is obviously happening at $h/c = 0.15$ as the foil approaches the symmetry plane in Fig. 12(b). The adverse pressure gradient has a rapid increase on the lower surface as the foil getting close to the symmetry plane, while the separation of boundary layer appears at about $t/T = 0.5$ (Molina and Zhang, 2011). However, the vortex does not leave from the lower surface immediately, it travels from the leading edge to the trailing edge and sheds until about $t/T = 0.625$, which do not induce an obvious stall during $t/T = 0.5$–0.625 because of the dynamic stall delay (Mckinney and Delaurier, 1981).

To have a further comparison of the numerical results between the two rotating shaft positions x_p, the corresponding average energy extraction power coefficient, average horizontal force coefficient and energy extraction efficiency with different h/c at $x_p = c/3$ and $c/2$ are given in Fig. 13.

In Fig. 13(a), compared with the results at $x_p = c/3$, the average horizontal force coefficient at $x_p = c/2$ is relatively small. As the gap h decreases to less than $0.25c$, the horizontal force coefficient increases significantly at $x_p = c/2$. In Fig. 13(b), when the gap is larger than $0.25c$,

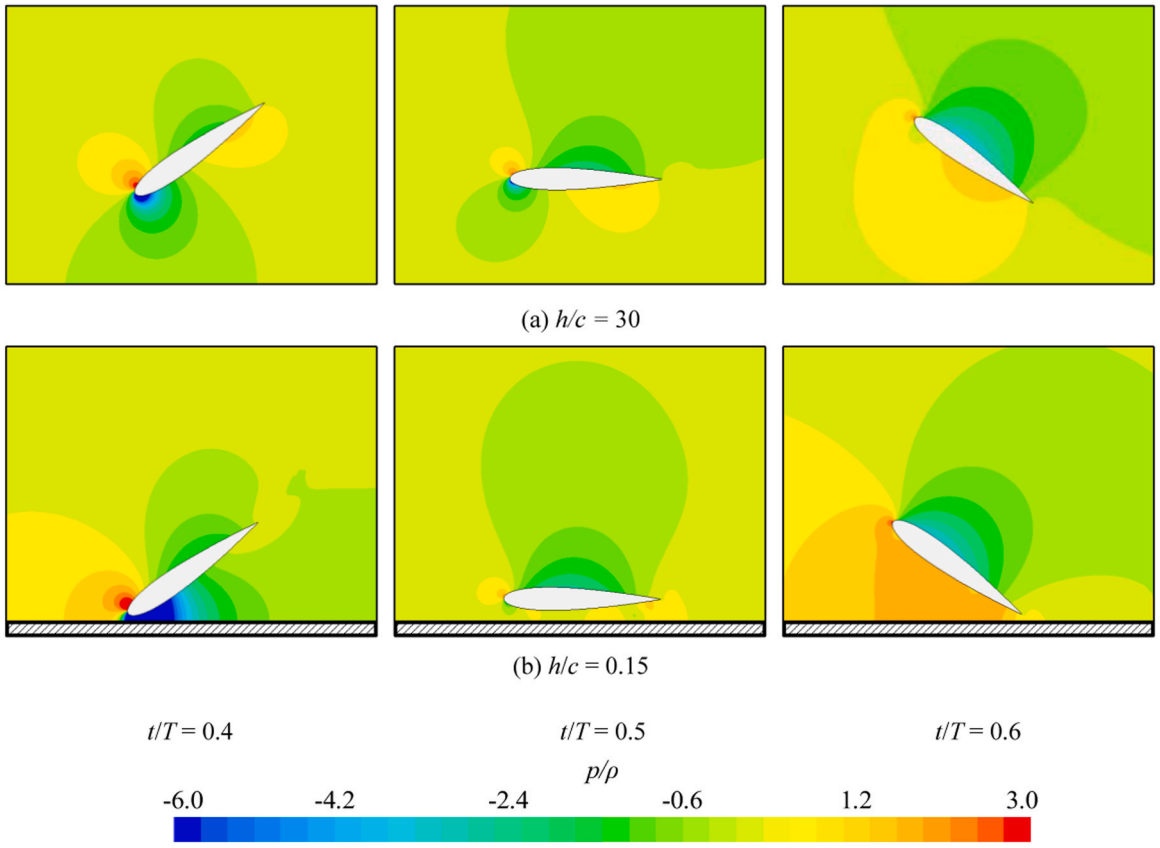

Fig. 10. Comparisons of pressure distribution among different gaps at $t/T = 0.4, 0.5, 0.6$. —NACA0015, $f^* = 0.14$, $\theta_0 = 60°$, $H_0 = c$, $Re = 500{,}000$, $x_p = c/2$.

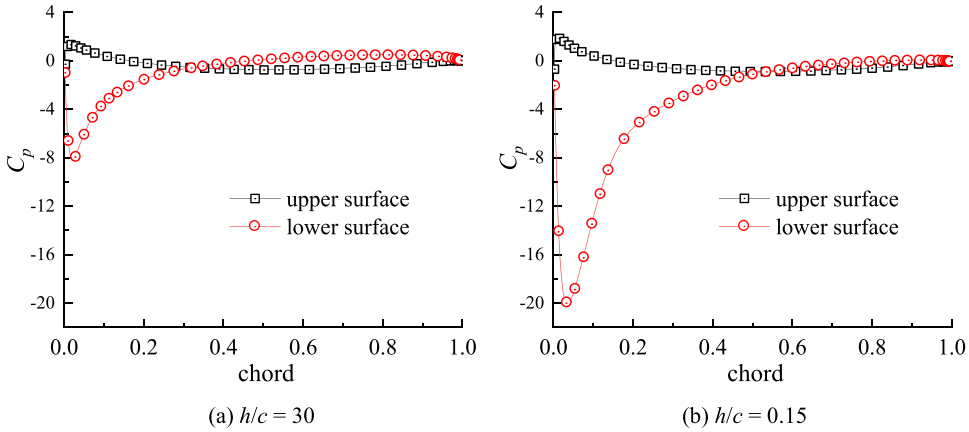

Fig. 11. Distribution of pressure coefficient on the surface of hydrofoil at $t/T = 0.4$.

the average power coefficient at the $x_p = c/3$ acquires higher values. As the gap h decreases to less than $0.25c$, the average power coefficient increases rapidly at $x_p = c/2$, which is caused by the Venturi effect. In Fig. 13(c), the efficiency has a steep increment at $x_p = c/2$ as the gap is smaller than $0.25c$. In contrast, the profile for $c/3$ is relatively stable. Moreover, the efficiency has an overall better result at $x_p = c/2$ benefit from a smaller swept area d.

5. Conclusions

The hydrodynamic performances of the flapping hydrofoils with/without the WIG effect are numerically studied using the CFD software STAR CCM+. The uncertainty analysis has been conducted in the validation section, proving that the numerical uncertainty in the present study is small enough to guarantee the accuracy of the model. The effects of the gap on the hydrodynamic performance of hydrofoils are analyzed, and the force coefficients and flow fields are compared.

When the gap h is larger than $0.25c$ at $x_p = c/3$, the improvement of power extraction efficiency is mainly attributed to the increase of the positive pressure on the lower surface when the foil gradually departs from the symmetry plane. This phenomenon is mainly caused by the blockage between the two foils. In this way, the efficiency has an increase of 6.79% at the gap $h/c = 0.25$ compared to a condition without the WIG effect at $h/c = 30$. The best performance is at the phase of 90° with a good combination of peak value and synchronization between vertical force and velocity.

When the hydrofoil has a closer distance to the symmetry plane at $x_p = c/2$, the WIG effect has a more significant impact on the power

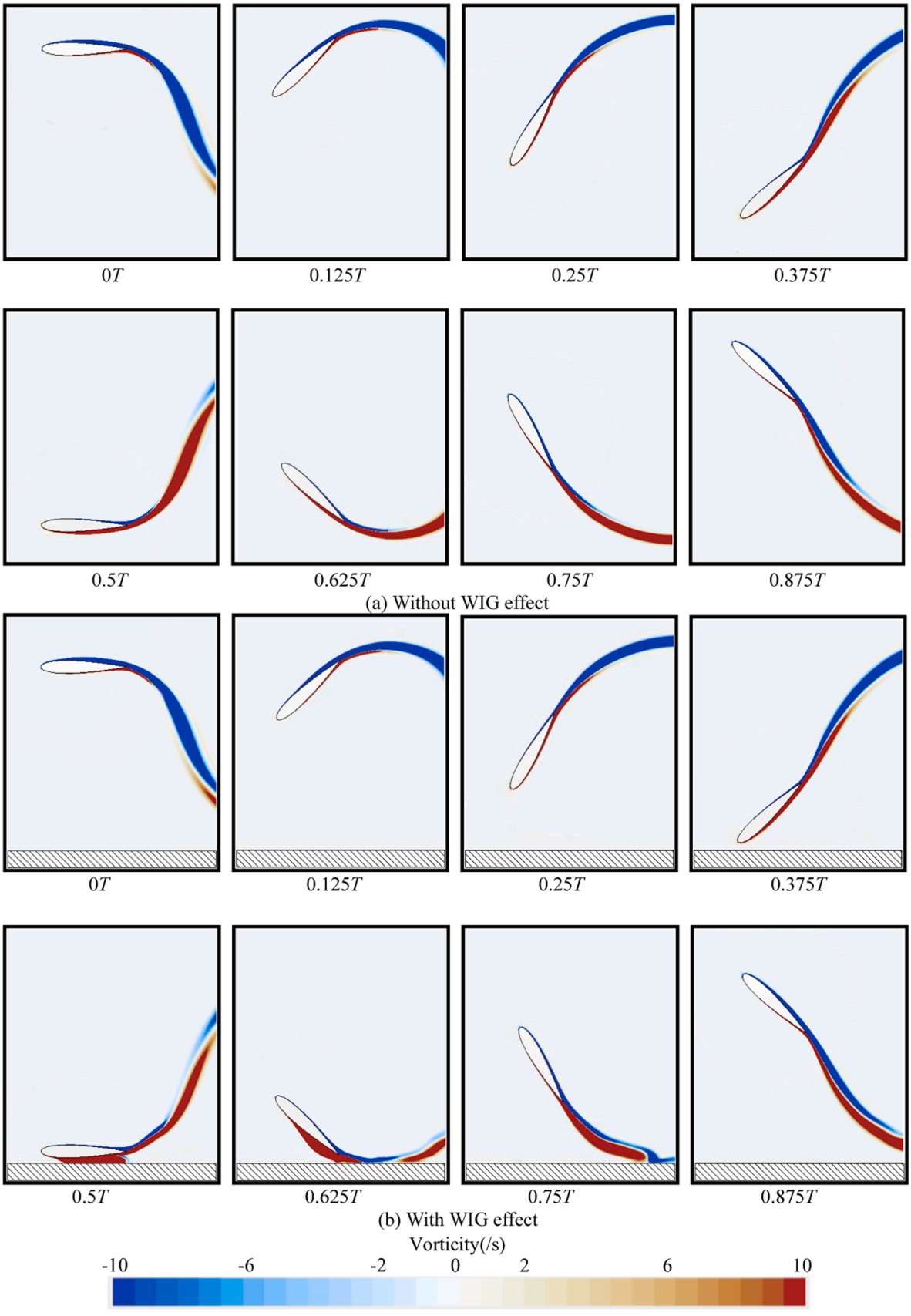

Fig. 12. Comparisons of vorticity distribution among two gaps $h/c = 30$ and 0.15 at eight instants. —NACA0015, $f^* = 0.14$, $\theta_0 = 60^\circ$, $H_0 = c$, $Re = 500{,}000$, $x_p = c/2$.

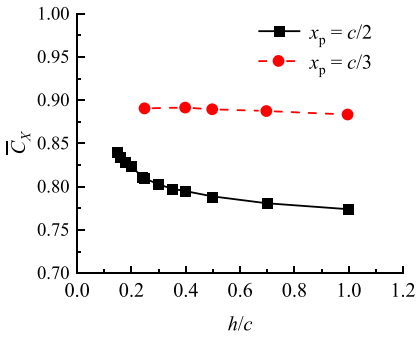

(a) Average horizontal force coefficients with different gaps at $x_p = c/2$ and $c/3$.

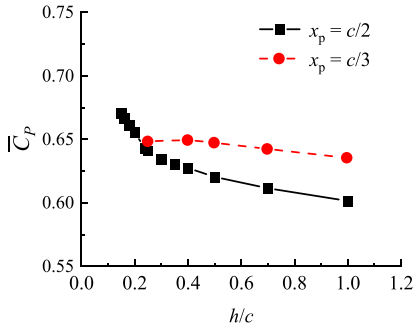

(b) Average power extraction coefficients with different gaps at $x_p = c/2$ and $c/3$.

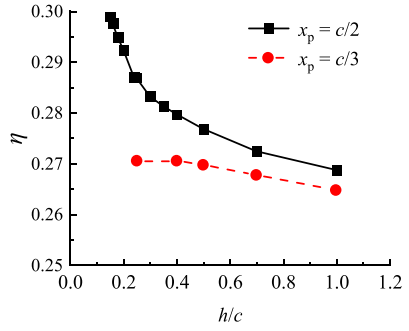

(c) Power extraction efficiencies with different gaps at $x_p = c/2$ and $c/3$.

Fig. 13. Comparisons of average power extraction coefficients and efficiencies between $x_p = c/3$ and $c/2$.

extraction by $\eta = 29.90\%$ at $h/c = 0.15$ with 16.34% increment. The suction side plays a dominant role improving the power extraction when the hydrofoil approaches the symmetry plane at $t/T = 0.40$–0.45 instead of a positive pressure in the departing process at $t/T = 0.5$–0.6. The Venturi effect occurs when the gap between the leading edge and the symmetry plane is very small, and it generates a local negative pressure area, further resulting in a separation of the boundary layer on the surface of hydrofoil due to a developed adverse pressure gradient. However, the vortex has not been departed from the lower surface immediately. In this regard, the power extraction improves largely. The WIG effect becomes weak when the gap h between the hydrofoil and symmetry plane is larger than one chord length c.

The present 2D numerical results are useful to reveal some physical mechanisms, which can provide some reference values for the further 3D study. Notably, the 2D numerical results obtained in this work cannot be directly extrapolated to 3D results as the 3D effect is neglected. We would like to conduct 3D numerical studies in our future work.

CRediT authorship contribution statement

Weijie Mo: Writing - original draft, Methodology. **Guanghua He:** Conceptualization, Supervision, Resources, Writing- reviewing and editing, Funding acquisition. **Jian Wang:** Methodology, Software, Formal analysis. **Zhigang Zhang:** Formal analysis. **Jiadong Wang:** Methodology. **Pengfei Liu:** Conceptualization and Methodology. **Hassan Ghassemi:** Supervision. **Hao Yang:** Software.

Declaration of Competing Interest

All authors declare that they have no conflict of interest.

Data availability

Data will be made available on request.

Acknowledgements

This work was supported by Taishan Scholars Project of Shandong Province (tsqn201909172), Fundamental Research Funds for the Central Universities, China (HIT.OCEF. 2021037), University young innovational team program, Shandong Province (2019KJN003).

References

Young, J., Lai, J.C.S., Platzer, M.F., 2014. A review of progress and challenges in flapping foil power generation [J]. Prog. Aerosp. Sci. 67, 2–28.
Mckinney, W., Delaurier, J., 1981. The Wingmill: An Oscillating-Wing Windmill [J]. J. Energy 5 (2), 109–115.
Jones, K.D., Platzer, M.F., 1997. Numerical computation of flapping-wing propulsion and power extraction[C]. AIAA Aerosp. Sci. Meet. Exhib.
Simpson, B. Experimental Studies of Flapping Foils for Energy Extraction, M.Sc. Thesis, Dept. of Mechanical Engineering, Massachusetts Inst. of Technology, Cambridge, MA, 2009.
Young, J., Ashraf, M.A., Lai, J.C., et al., 2013. Numerical simulation of fully passive flapping foil power generation [J]. AIAA J. 51 (11), 2727–2739.
Deng, J., Caulfield, C.P., Shao, X., 2014. Effect of aspect ratio on the energy extraction efficiency of three-dimensional flapping foils [J]. Phys. Fluids 26 (4), 041101–041594.
Kinsey, T., Dumas, G., 2008. Parametric study of an oscillating airfoil in a power-extraction regime [J]. AIAA J. 46 (6), 1318–1330.
Kinsey, T., Dumas, G., Lalande, G., et al., 2011. Prototype testing of a hydrokinetic turbine based on oscillating hydrofoils [J]. Renew. Energy 36 (6), 1710–1718.
Kinsey, T., Dumas, G., 2012. Computational fluid dynamics analysis of a hydrokinetic turbine based on oscillating hydrofoils [J]. J. Fluids Eng. 134 (2), 021104.
Kinsey, T., Dumas, G., 2014. Optimal operating parameters for an oscillating foil turbine at Reynolds number 500,000 [J]. AIAA J. 52 (9), 1885–1895.
Picard-Deland, M., Olivier, M., Dumas, G., et al., 2019. Oscillating-foil turbine operating at large heaving amplitudes [J]. AIAA J. 57 (1), 1–10.
Xu, G.D., Xu, W., 2017. Energy extraction of two flapping foils with tandem configurations and vortex interactions [J]. Eng. Anal. Bound. Elem. 82 (sep.), 202–209.
Kinsey, T., 2012. Optimal tandem configuration for oscillating-foils hydrokinetic turbine [J]. J. Fluids Eng. 134 (3), 031103.
Duarte, L., Dellinger, N., Dellinger, G., Ghenaim, A., Terfous, A., 2019. Experimental investigation of the dynamic behaviour of a fully passive flapping foil hydrokinetic turbine. J. Fluids Struct. 88, 1–12.
Duarte, L., Dellinger, G., Dellinger, N., Ghenaim, A., Terfous, A., 2021. Implementation and validation of a strongly coupled numerical model of a fully passive flapping foil turbine. J. Fluids Struct. 102, 103248.
Theodorakis, K., Ntouras, D., Papadakis, G., 2022. Investigation of a submerged fully passive energy-extracting flapping foil operating in sheared inflow. J. Fluids Struct. 113, 103674.
The Engineering Business Limited, 2002. Research and development of a 150kw tidal stream generator. Tech. rep., Crown Copyright.
The Engineering Business Limited, 2003. Stingray tidal energy device - phase2. Tech. rep., Crown Copyright.
The Engineering Business Limited, 2005. Stingray tidal energy device - phase3. Tech. rep., Crown Copyright.
Pulse Tidal Ltd, 2011. www.plusetidal.com.
Luo, S.C., Chen, Y.S., 2012. Ground effect on flow past a wing with a NACA0015 cross-section [J]. Exp. Therm. Fluid Sci. 40, 18–28.
Molina, J., Zhang, X., 2011. Aerodynamics of a heaving airfoil in ground effect [J]. Aiaa J. 49 (6), 1168–1179.
Jones K.D., Platzer M.F. A numerical and experimental investigation of flapping-wing propulsion in ground effect - 40th AIAA Aerospace Sciences Meeting & Exhibit (AIAA) [J]. 2002.
Liu, P., Wang, T., Huang, G., et al., 2010. Propulsion characteristics of wing-in-ground effect dual-foil propulsors [J]. Appl. Ocean Res. 32 (1), 103–112.
Wang, J., Liu, P., Chin, C., et al., 2020. Parametric study on hydro-elasticity characteristics of auto-pitch wing-in-ground effect oscillating foil propulsors [J]. Ocean Eng. 201, 107115.

Zhu, Q., Haase, M., Wu, C.H., 2009. Modeling the capacity of a novel flow-energy harvester [J]. Appl. Math. Model. 33 (5), 2207–2217.
Liu, Pengfei, 2015. WIG (wing-in-ground) effect dual-foil turbine for high renewable energy performance [J]. Energy 83, 366–378.
Moryossef, Y., Levy, Y., 2004. Effect of oscillations on airfoils in close proximity to the ground [J]. Aiaa J. 42 (9), 1755–1764.
Zhu, B., Zhang, J., Zhang, W., 2020. Impact of the ground effect on the energy extraction properties of a flapping wing [J]. Ocean Eng. 209, 107376.
Abiru H., Yoshitake A. Experimental Study on a Cascade Flapping Wing Hydroelectric Power Generator[C]. 2012: 1429-1436.
Zerihan J. An investigation into the aerodynamics of wings in ground effect [D]. University of Southampton, 2001.
Nishino, T., Roberts, G.T., Zhang, X., 2008. Unsteady RANS and detached-eddy simulations of flow around a circular cylinder in ground effect [J]. J. Fluids Struct. 24 (1), 18–33.
Kinsey, T., Dumas, G., and Olivier, M. "Heaving Amplitude Effects on Oscillating Wing Turbines," Proceedings of the 15th Annual Conference of the CFD Society of Canada, CFD Society Paper 20071068, 2007.
Zhu, Q., 2011. Optimal frequency for flow energy harvesting of a flapping foil [J]. J. Fluid Mech. 675, 495–517.
Stern, F., Wilson, R.V., Coleman, H.W., et al., 2001. Comprehensive approach to verification and validation of CFD simulations. Part 1: methodologies and procedures [J]. Fluid Eng. 123 (4), 793–802.
Wilson, R.V., Stern, F., Coleman, H.W., et al., 2001. Comprehensive approach to verification and validation of CFD smulations. Part 2: application for rans simulation of a cargo/container ship [J]. J. Fluid Eng. 123 (4), 803–810.
Stern, F., Wilson, R., Shao, J., 2010. Quantitative V&V of CFD simulations and certification of CFD codes [J]. Int. J. Numer. Methods Fluids 50 (11), 1335–1355.
Wu, J., Shu, C., Zhao, N., et al., 2014. Fluid dynamics of flapping insect wing in ground effect[J]. J. Bionic Eng. 11 (1), 52–60.
Su, Y., Miller, M., Mandre, S., et al., 2018. Confinement effects on energy harvesting by a heaving and pitching hydrofoil [J]. J. Fluids Struct. 84, 233–242.